Hydrothermal pressure-temperature control on CO_2 emissions and seismicity at Campi Flegrei (Italy)

G. Chiodini[1,*], S. Caliro[2], R. Avino[2], G. Bini[3], F. Giudicepietro[2], W. De Cesare[2], P. Ricciolino[2], A. Aiuppa[4], C. Cardellini[5,1], Z. Petrillo[2], J. Selva[1], A. Siniscalchi[6], S. Tripaldi[6]

[1] Istituto Nazionale di Geofisica e Vulcanologia, Sezione di Bologna, via D. Creti 12, 40128 Bologna, Italy.
[2] Istituto Nazionale di Geofisica e Vulcanologia, Sezione di Napoli Osservatorio Vesuviano, via Diocleziano 328, 80124 Napoli, Italy.
[3] Institute of Geochemistry and Petrology, ETH Zürich, Clausiusstrasse 25, 8092 Zürich, Switzerland
[4] Dipartimento di Scienze della Terra e del Mare (DiSTeM), Università degli Studi di Palermo, via Archirafi 22, 90123 Palermo, Italy.
[5] Dipartimento di Fisica e Geologia, Università degli Studi di Perugia, via Pascoli snc, 06123 Perugia, Italy.
[6] Dipartimento di Scienze della Terra e Geoambientali Università degli Studi di Bari - Aldo Moro, via Edoardo Orabona, 4, 70125 Bari, Italy.

*corresponding author: giovanni.chiodini@ingv.it

Highlights

- Gas-geoindicators indicate an escalation of the hydrothermal P-T Campi Flegrei
- Pressurization causes increase of the CO_2 emission at Solfatara (up to 5000 t/d)
- Increasing hydrothermal P-T and CO_2 emission trigger low magnitude earthquakes

Abstract

Fluids supplied by stored magma at depth are causal factors of volcanic unrest, as they can cause pressurization/heating of hydrothermal systems. However, evidence for links between hydrothermal pressurization, CO_2 emission and volcano seismicity have remained elusive. Here, we use recent (2010-2020) observations at Campi Flegrei caldera (CFc) to show hydrothermal pressure, gas emission and seismicity at CFc share common source areas and well-matching temporal evolutions. We interpret the recent escalation in seismicity and surface gas emissions as caused by pressure-temperature increase at the top of a vertically elongated (0.3-2 km deep) gas front. Using mass (steam) balance considerations, we show hydrothermal pressurization is causing energy transfer

from the fluids to the host rocks, ultimately triggering low magnitude earthquakes within a seismogenetic volume containing the hydrothermal system. This mechanism is probably common to other worldwide calderas in similar hydrothermal activity state.

Keywords
Volcanic unrest, hydrothermal systems, Campi Flegrei, fumarole compositions, CO_2 emission, volcano seismicity

1. Introduction

The injection, ascent, storage and surface release of deep fluids in the upper crust are widespread phenomena in nature, and are recurrent drivers of geological catastrophes. Fluid pressure increase in the upper crust can trigger seismicity reducing the effective normal stress on fault planes (e.g., Hubbert and Rubey, 1959; Sibson, 1992; Miller, 2013), and the recurrently observed co-seismic variations in gas flux and composition (Fischer et al., 2017; Girault et al., 2018; Chiodini et al., 2020) are clear hints for a cause-effect link between fluids and earthquakes. It is also well-established that artificial fluid injection in the subsurface, and the consequent fluid pressure increase, can lead to seismicity (Ellsworth, 2013; Keranen and Weingarten, 2018).
Volcanoes make no exception, the most notable example being that of Mammoth Mt. (California), when the sudden surface burst (in 1990) of huge amounts of volcanic-hydrothermal CO_2 associated to a seismic crisis killed a large portion of the forest (Farrar et al., 1995; Sorey et al., 1998), and repeated increases in diffuse CO_2 emissions accompanied seismic swarms in the subsequent years (Lewicki et al., 2014; Werner et al., 2014; Hotovec-Ellis et al., 2018; Pfeiffer et al., 2018).
Volcanoes are especially suitable natural laboratories for investigating fluid flow - pressure - earthquake associations, because robust and relatively continuous geochemical and geophysical datasets are available. One aspect that is especially relevant to restless volcanoes is that injected fluids are generally hot and H_2O-rich so that, upon ascent, can interact with, and condense into, hydrothermal aquifers: the heating and consequent volumetric expansion of the hosting rocks that

63 result from condensation of such magmatic steam is a potential additional seismicity driver during
64 volcanic unrest (Chiodini et al., 2015).
65 The relations among hydrothermal temperature-pressure, fluid flow and earthquakes are here
66 investigated at Campi Flegrei (CFc, Fig. 1a), a restless resurgent caldera formed ~ 39 kyrs ago by
67 the largest caldera-forming eruption in Europe in the last 200 kyrs (Costa et al., 2012). CFc exhibits
68 (since the 1950s) repeated inflation periods (Orsi et al., 1999; Del Gaudio et al., 2010) and seismic
69 crises, which have worried the scientific community as much to suggest an eruption is approaching
70 (Selva et al., 2012; Kilburn et al., 2017). The CFc is undergoing since 2004 a new inflation phase
71 (total maximum vertical displacement of ~ 0.75 m by the time of writing), associated with frequent
72 shallow seismicity, part of which interpreted as originating from fluid transfer processes (Bianco et
73 al., 2004; Saccorotti et al., 2007; D'Auria et al., 2011; Chiodini et al., 2017a; Giudicepietro et al.,
74 2020). At the same time, large compositional variations are being observed in the fumarolic
75 effluents (Caliro et al., 2014; Chiodini et al., 2016), and marked flux increases are being registered
76 in hydrothermal CO_2 release from both fumarolic vents (Tamburello et al., 2019) and soil diffuse
77 degassing structures (Cardellini et al., 2017). The escalating CO_2 emissions, and the concomitant
78 compositional changes in the fumaroles, have been interpreted as signs that magma degassing at
79 depth may have reached a critical condition in which heating and pressurization of the shallower
80 CFc hydrothermal system is occurring at accelerating rate (Caliro et al., 2014; Chiodini et al., 2015;
81 2016). In 2012, the evolution of the monitored geophysical and geochemical parameters induced the
82 Italian Civil Protection (DPC) to raise the CFc alert level from green (calm) to yellow (attention).
83 Here, we characterise the recent pressure-temperature (P-T from here on) evolution in the CFc
84 hydrothermal system, as inferred from geochemical modelling of fumarolic compositions, and to
85 explore its temporal link with the rates of deeply derived CO_2 emissions and seismicity. To this
86 aim, our multidisciplinary analysis combines results for the chemical compositions of the CFc
87 fumaroles with a set of variables related to the gas emission, and the earthquakes. We exclude from

our analysis the deformation signals, as their main source area is thought to be deeper than the hydrothermal system this work is focussed on (3-4 km; Amoruso et al., 2014a; 2014b).

Geochemical data (fumarolic compositions and CO_2 fluxes) refer to the hydrothermal sites of Solfatara and Pisciarelli (Fig. 1). Solfatara, a tuff cone formed about 4 ka ago (Smith et al., 2011), is the most active degassing zone of the CFc, being site of numerous fumarolic vents and of a widespread soil diffuse degassing of hydrothermal-volcanic CO_2 (Chiodini et al., 2001; Cardellini et al., 2017; Fig. 1b). The most recent CO_2 flux measurements performed over the entire zone identify a ~ 1 km^2 wide area diffusively emitting deeply derived CO_2 (the so called Solfatara Diffuse Degassing Structure, Solfatara DDS, Chiodini et al., 2001; Fig. 1b). The typical CO_2 flux sustained by the DDS was 1000-2000 t d^{-1} in 2014-2016 period (Cardellini et al., 2017). Significant amounts of CO_2 are also emitted by fumarolic vents, the most active of which are located in the eastern slope of the Solfatara cone (Pisciarelli vents, CO_2 emission up to 600 t d^{-1} in 2019 (Tamburello et al., 2019) and inside the Solfatara depression (BG and BN vents, CO_2 emission up to ~ 300 t d^{-1} in 2013; Aiuppa et al., 2013; Pedone et al., 2014; Fig. 1b).

After a description of the evolution over time of different parameters we attempt an integrated analysis aimed at understanding the impact of hydrothermal fluid P-T changes on earthquakes occurrence and fluid emissions.

2. Databases

The databases used in this work (Supplementary Data File S1) are here briefly described.

2.1. Chemical compositions of Solfatara fumaroles.

The main and hottest fumaroles of Solfatara, BG (T=150-165°C) and BN (T 140-150°C) (Fig. 1b), have been systematically sampled since 1983 and 1995, respectively. The dataset includes the temperature and chemical compositions (H_2O, CO_2, H_2S, Ar, N_2, H_2, CH_4 and CO) of gas samples

taken and analysed with similar procedures, from 1983 to 2020 (see Caliro et al., 2007; Cioni and Corazza, 1981 for the sampling and analytical methods). This Solfatara fumarolic fluid database is unique for the large number of samples (671), for its continuity (~ 35 years of observations) and for the homogeneity of the sampling and analytical methods used. Different laboratories contributed to this database: the laboratories of CNR of Pisa that started the work at the beginning of 1980's; the laboratory of University of Perugia that analysed the gas samples in the middle 1990's; and the fluid geochemistry laboratory of Osservatorio Vesuviano from 1998 to 2020.

2.2. Diffuse CO_2 flux from the Solfatara crater target area.

During April 2004 - October 2020, 149 soil CO_2 flux campaigns have been performed inside the Solfatara crater. In total, the dataset consists of 9315 measurements performed with the accumulation chamber method (Chiodini et al., 1998) over a grid of 63 points whose location remained unchanged during the period (Fig. 1b). The data are reported in monthly surveillance reports of Osservatorio Vesuviano for the Civil Defence of Italy (http://www.ov.ingv.it/ov/it/bollettini/275.html). The results of the first 50 campaigns have already been published (Granieri et al., 2009), while the remaining are here reported for the first time. For each campaign, we computed the total CO_2 output (FCO2 in t d^{-1}) from the target area (Fig. 1b). The FCO2 and its uncertainty were computed by applying a geostatistical method based on sequential Gaussian simulation (sGs; Cardellini et al., 2003) to the soil CO_2 fluxes of the 149 campaigns. Specifically, we used the *sgsim* algorithm (GSLIB software library; Deutsch and Journel, 1998). The CO_2 flux has been simulated on a of 4 × 4 grid m starting from variogram models fitting the experimental variograms of the normal scores of the CO_2 flux (for further details see Cardellini et al., 2003). For each campaign, 200 simulations were realised and the total CO_2 release was computed by summing the products of the simulated CO_2 flux value at each grid cell by the cell surface. The mean total CO_2 flux and its standard deviation, computed from the 200

138 realizations, are taken as FCO2 and its uncertainty for each campaign. As an example,
139 Supplementary Fig. S1 illustrates the CO_2 flux map obtained considering at each location the mean
140 of the CO_2 fluxes measured in the 149 campaigns. The target area to which each FCO2 estimate
141 refers to (coloured area in Supplementary Fig. S1) was limited to the area within the outermost
142 measuring points, in order to avoid uncertainties related to extrapolations to un-sampled zones.

143

144 ***2.3. Diffuse CO_2 flux from the Solfatara DDS.***

145 This dataset includes the total CO_2 output by diffuse degassing at Solfatara (FCO2-DDS) from 1998
146 to 2016 estimated from soil CO_2 flux measurements covering an area of 1.4 km^2 which includes
147 Solfatara crater and Pisciarelli areas (Fig. 1b; Cardellini et al., 2017). The soil CO_2 fluxes were
148 measured in 30 surveys using the accumulation chamber method (Chiodini et al., 1998) and the
149 total CO_2 output was estimated applying a geostatistical method based on sGs (for further details
150 see Cardellini et al., 2017).

151

152 ***2.4. CO_2 fluxes from Pisciarelli vents.***

153 This dataset is composed of twenty-one measurements of the CO_2 flux from the Pisciarelli vents
154 performed by different authors during 2012-2019 (Aiuppa et al., 2013; Pedone et al., 2014; Aiuppa
155 et al., 2015; Queißer et al., 2017; Tamburello et al., 2019). Measurement methods are different and
156 include: tunable diode laser absorption spectroscopy (Pedone et al., 2014), differential absorption
157 lidar (Aiuppa et al., 2015), laser remote-sensing spectrometry (LARSS; Queißer et al., 2017), multi-
158 component gas analyzer system (MultiGAS; Aiuppa et al., 2013; Tamburello et al., 2019). The
159 reader is referred to the original articles for the details on these different techniques. Tamburello et
160 al. (2019) report an overall consistency of the CO_2 fluxes obtained with the different measurement
161 methods.

2.5. Fumarolic tremor at Pisciarelli.

The fumarolic tremor is a continuous seismic signal recorded in the vicinity of the Pisciarelli fumaroles, currently the largest of the CFc. To record this signal, a seismic station was installed in 2010 about 8 m away from the main fumarolic vent. The fumarolic tremor, analyzed in previous studies (Chiodini et al., 2017b; Giudicepietro et al., 2019; 2020), is polarized in the vertical direction and characterized by a spectral peak at around 10 hz. To represent the temporal evolution of the tremor amplitude, the Real-time Seismic-Amplitude Measurement (RSAM; Endo and Murray, 1991) was calculated on 30-minute windows of the vertical component signal, filtered in 5 -15 Hz frequency band.

2.6. Air CO_2 concentrations at Pisciarelli.

Since April 2007, an automatic station measures soil temperature, soil CO_2 fluxes, and CO_2 concentrations in air, at 40 cm height, 20 m downwind of the main Pisciarelli vent (Chiodini et al., 2017b). The April 2007-October 2020 daily air CO_2 concentrations are systematically higher than in ambient air (1000-5000 ppm vs ~ 400 ppm) due to persistent fumigation from the fumarolic plume.

2.7. Earthquakes

We used the CFc earthquake locations available in the public-access INGV- Osservatorio Vesuviano database (http://sismolab.ov.ingv.it/sismo/index.php?PAGE=SISMO/last&area=Flegrei). Hypocentre locations were obtained using a 1D layered velocity model. The dataset consists of 2026 located earthquakes with magnitude (Md) ranging between -1.1 and 3.3, representing about 47% of the total number of CFc earthquakes recorded by the INGV-Osservatorio Vesuviano permanent seismic

network between January 2004 and October 2020. Seismicity is mostly concentrated in the Solfatara-Pisciarelli area (Fig. 1a) at relatively shallow depth and the magnitude of the events is generally low with only 16 events with $2.0 \leq Md \leq 3.3$. From 2005 to 2012, earthquakes occurred mainly in swarms. Since 2012-2013, their occurrence rate has increased over time, both as swarms and as single events, with single events becoming more frequent in the last 2 years.

3. Results and Discussion

3.1. Pressure-temperature geoindicators based on fumarole compositions

Solfatara fumaroles emit vapours characterised by the absence of acidic gas species (i.e., SO_2, HCl, HF) that are typical of high-temperature magmatic gas emissions. They also exhibit detectable amounts of species formed in the hydrothermal environment (e.g., CH_4). These compositions suggest fumarolic steam originates from a hydrothermal system in which the original magmatic acidic components have already been removed by scrubbing processes (Cioni et al., 1984; Caliro et al., 2007). Since 1984, the Solfatara compositional database was used to derive the T-P conditions of this hydrothermal system (e.g., Cioni et al., 1984; Chiodini et al., 1996; Caliro et al., 2007; Chiodini et al., 2015; Chiodini et al., 2016). Recently, two different geochemical approaches have lead to contrasting results and different implications for the current CFc unrest, which has been interpreted as either driven by pressurization of the CFc system (Chiodini et al., 2015; 2017a), or associated with a general depressurization of the hydrothermal system (Moretti et al., 2017) (Fig. 2). We refer to the two approaches, which stand on different model assumptions, as the *no-condensation* (Moretti et al., 2017) and *vapour-liquid coexistence* (Chiodini et al., 2015) models.

3.1.1. The no-condensation model

Moretti et al. (2017) applied a model originally developed by Chiodini et al., (1996) and then refined by Chiodini and Marini (1998). The geobarometric and geothermometric relations are

211 derived considering the formation reactions of H_2, CO and CH_4 from the main species H_2O and
212 CO_2:

213 $$H_2O \leftrightarrow H_2 + 1/2\ O_2 \quad (1)$$

214 $$CO_2 \leftrightarrow CO + 1/2\ O_2 \quad (2)$$

215 $$CO_2 + 2\ H_2O \leftrightarrow CH_4 + 2\ O_2 \quad (3)$$

216 whose equilibrium constants are expressible as:

217 $$\log K_{H2} = \log f_{H2} + 1/2 \log f_{O2} - \log f_{H2O} \quad (4)$$

218 $$\log K_{CO} = \log f_{CO} + 1/2 \log f_{O2} - \log f_{CO2} \quad (5)$$

219 $$\log K_{CH4} = \log f_{CH4} + 2 \log f_{O2} - \log f_{CO2} - 2 \log f_{H2O} \quad (6)$$

220 where $\log K_{H2} = -12707/T + 2.548$, $\log K_{CO} = -14955/T + 5.033$ and $\log K_{CH4} = - 42007/T + 0.527$
221 (thermodynamic data from Stull et al., 1969). Suitable combinations of equations 4, 5 and 6 allow
222 to eliminate the $\log f_{O2}$ variable and to derive the following geothermometric and geobarometric
223 functions:

224 $$T = -2248 / (\mathrm{Log}\ (X_{CO}/X_{CO2}) + \mathrm{Log}\ (X_{H2O}/X_{H2}) - 2.485) \quad (7)$$

225 $$\mathrm{Log}\ P_{H2O} = (19.605 - \mathrm{Log}\ (X_{CO}^4/(X_{CH4} \times X_{CO2}^3)) - 17813/T)/2 \quad (8)$$

226 where the equimolar ratios of the measured fumarolic molar fractions (X_i) are assumed equal to the
227 fugacities ratios and $P_{H2O} \sim f_{H2O.}$.

228 Finally considering the Dalton law,

229 $$P_{CO2} = P_{H2O}\, X_{CO2} / X_{H2O} \quad (9)$$

230 $$Ptot \sim P_{CO2} + P_{H2O.} \quad (10)$$

231 Relevant assumptions of this approach are: (i) the redox conditions are internally fixed within the
232 H_2O-CO_2-H_2-CO- CH_4 gas system, an assumption that implies that CH_4 equilibrates at the same T-
233 P conditions as the kinetically faster species H_2 and CO (Giggenbach, 1987); (ii) no secondary
234 processes affect H_2O (condensation and/or water addition). Because the contrasting results with the
235 model of Chiodini et al. (2015) strongly depends on this last assumption, we name the model used
236 by Moretti et al. (2017) as the *no-condensation* model.

237

238 ***3.1.2. The vapor-liquid coexistence model***

239 Caliro et al. (2007), showed in a log H_2/H_2O vs log CO/CO_2 stability diagram (Fig. 5 in Caliro et
240 al., 2007) that Solfatara fumaroles plot close to a typical hydrothermal redox buffer (DP; D'Amore
241 and Panichi, 1980) at temperature of 200-250°C and far from the H_2S-SO_2 redox buffer of volcanic
242 gases (Giggenbach, 1987). The same authors, considering the carbon isotopic exchange reaction
243 between CO_2 and CH_4, demonstrated that the CH_4/CO_2 ratio reflects temperatures (360-430°C)
244 much higher than those returned by the H_2/H_2O and CO/CO_2 ratios, a fact that in principle excludes
245 the possibility of using CH_4, CO and H_2 in a unique geothermometric function. Furthermore,
246 starting from early 2000's, macroscopic evidences suggested the occurrence of secondary processes
247 (i.e., steam condensation) affecting the fumarolic H_2O content: (i) the almost continuous increase in
248 the non-condensable gas fraction relative to water (Chiodini et al., 2015); (ii) a systematic increase
249 of the CO/CO_2 ratio (an indicator of hydrothermal temperature, and condensation is very efficient to
250 heat a hydrothermal system); (iii) the pervasive circulation of condensates underneath Solfatara
251 crater, and in particular close to the main fumaroles BG and BN (Bruno et al., 2007; Byrdina et al.,
252 2014; Gresse et al., 2017); (iv) the formation of strong boiling pool of condensates and repeated
253 episodes of liquid/mud emission at Pisciarelli (Chiodini et al., 2015).
254 In order to avoid the effects of these secondary processes affecting H_2O, and in order to exclude
255 CH_4 from the model, Chiodini et al. (2015) derived T-P functions from equations 4 and 5 based on
256 equimolar ratios between non-condensable gases (H_2, CO, CO_2). The derivation of the
257 geothermometric and geobarometric function was possible considering (i) f_{H2O} fixed by the vapour-
258 liquid coexistence and (ii) f_{O2} as a function of the temperature. Redox conditions of Solfatara gases
259 were assumed to be controlled by the DP buffer (log f_{O2} = 8.20 - 23643/T). According to Chiodini
260 and Marini (1998), an alternative f_{O2}-T function applicable to Solfatara fumarolic gases is the
261 'Campanian Volcanoes' buffer (CV, log f_{O2} = 7.75 - 23169/T). The correspondent geothermometric
262 relations are:

263 $T = 3133.5 / (0.933 - \text{Log } X_{CO}/X_{CO2})$ (11)

264 valid for redox conditions controlled by the DP relation, and

265 $T = 3370.5 / (1.158 - \text{Log } X_{CO}/X_{CO2})$ (12)

266 when considering the CV redox buffer.

267 The geobarometric functions are:

268 $\text{Log } P_{H2O} = 5.510 - 2048/T$ (13)

269 where the water pressure is assumed equal to water fugacity of saturated vapor (i.e., vapor-liquid

270 coexistence for pure water (Giggenbach, 1980)),

271 $\text{Log } P_{CO2} = 3.025 + 201/T - \text{Log } X_{H2}/X_{CO}$ (14)

272 derived by a linear combination of equations 4 and 5, and

273 $Ptot \sim P_{CO2} + P_{H2O.}$ (15)

274 Use of either the DP or the CV f_{O2}-T relation results into different P-T estimations. In agreement

275 with Chiodini et al. (2015), we use the DP option (equation 11) that, for the post 2010 period

276 considered in this work (see Fig. 6), outputs T values from 218°C to 267°C and P from 27 to 60 bar;

277 while the alternative equation 12 (CV buffer) returns higher T and P values (238°C - 287°C, 37 bar

278 - 78 bar). We stress, however, that these systematic differences do not affect the results and

279 considerations of our work that is based on the relative variation of the normalised T-P values that

280 are practically the same for both the DP and CV estimations.

281 We will refer to this model as the *vapour-liquid coexistence* model.

282

283 ***3.1.3. Temperature-Pressure estimations***

284 The T-P estimates, derived by the two models for the entire Solfatara fumaroles' database, are

285 contrasted in the chronograms of Fig. 2.

286 Even though, any model can not be considered completely reliable because it is necessarily based

287 on some a-priori assumptions, the *no-condensation model* is certainly not reliable because the total

288 estimated pressures (Ptot = P_{H2O} + P_{CO2}) for the post-2015 samples are impossible as systematically
289 below atmospheric pressure (<1 bar, Fig. 2b).
290 The reliability of the *vapour-liquid coexistence* model is tested below by comparing the inferred P-
291 T conditions with different independent fluid flow related variables, and with the earthquake
292 occurrence at CFc.
293
294 **3.2. Fluid flow related (FFR) variables**
295 Figures 3a, b ,c, d and e are chronograms of the available FFR variables that we take as proxies for
296 the CO_2 degassing regime of the Solfatara-Pisciarelli area. In particular the CO_2 flux (FCO2, Fig.
297 3a) from the Solfatara target area (see Fig. 1b) and the total CO_2 flux from the entire Solfatara DDS
298 (FCO2-DDS, Fig. 3b; Cardellini et al., 2017) are representative of the diffuse emission. Numerous
299 FCO2 data (149) are available for the entire observation period (2004-2020) while FCO2-DDS
300 measurements are less frequent (Cardellini et al., 2017) and not available since 2017.
301 The CO_2 flux from Pisciarelli vents (Fig. 3c; Tamburello et al., 2019), the fumarolic tremor at
302 Pisciarelli (RSAM, Fig. 3d) and the CO_2 concentrations in air at Pisciarelli (air CO_2, Fig. 3e) are
303 taken as proxies of the vent emission in the area. Although not direct flux measurements, RSAM
304 and air CO_2 are almost continuously acquired, and their temporal fluctuations have previously been
305 shown to scale with the intensity of hydrothermal activity at Pisciarelli (Fig. 4; Chiodini et al.,
306 2017b; Giudicepietro et al., 2019; 2020).
307
308 **3.3. 2004-2020 earthquakes occurrence at CFc**
309 We refer here to the earthquakes occurred at CFc from 2004 to October 2020 (Fig. 1a) whose
310 locations and magnitudes are available in public databases of the Osservatorio Vesuviano
311 (http://www.ov.ingv.it/ov/it/banche-dati.html; see Material and Methods). It is worth to note that
312 the events concentrate underneath the Solfatara-Pisciarelli (Fig. 1a) and are in general of low
313 magnitude (maximum magnitude = 3.3) and of relatively shallow depths (Fig. 5a). The earthquakes'

occurrence rate manifestly increases since 2017-2018 (Fig. 5b). Note that Fig. 5b reports events with magnitude ≥ 0.1, for which the catalogue is reasonably complete in the observation period. The absence of deep events at CFc (i.e., depth >3-4 km) likely reflects the high temperatures expected at depth, and a very shallow brittle-ductile transition (3-5 km; Castaldo et al., 2019).

3.4. Comparison of the different datasets

A multivariate time-series analysis is attempted to compare the different observations. To this aim, we compute the annual mean (annual number for the earthquakes) of each variable (red points in Figs. 2, 3 and 5), focussing on the 2010-2020 period, for which most of the variables are available. The approach based on the analysis of the annual values has the advantage of filtering out any seasonally controlled variations. The multivariate analysis is not applied to the FCO2-DDS (Fig. 3b) and to the CO_2 flux from Pisciarelli vents *(*Fig. 3c) because these measurements are sporadic and not available for the entire period. In detail, a Principal Component Analysis (PCA; Everitt et al., 2011; James et al., 2013) was performed on the annual means of the other FFR variables (air CO_2, FCO2, RSAM) and the annual number of earthquakes to simplify and summarize the relationships among the multivariate set of data. We used the function *prcomp* of the package *stats* of the R software (R Core Team, 2021), which performs PCA via a singular value decomposition of the centered and scaled data matrix. This technique derives a new set of uncorrelated variables (Principal Components, PC) using a linear combination of the original variables, and ranks them in terms of their overall control on the variance. PCA is therefore used to reduce the dimensionality of the data set, by choosing only those PCs that explain most of the variance in the data. In practice, the PCA applied to the 4-variables matrix returns 4 PC, which retain different proportions of the total variance: PC1 the 93.6%, PC2 the 3.9%, PC3 the 1.8%, and PC4 the 0.7% (Table 1). The scores of these new variables are calculated multiplying the matrix of the scaled original variables by the eigenvector matrix in Table 1 (namely, the eigenvectors of the correlation matrix of the original data set). These results indicate that nearly the total (temporal) variability of the data

340 (~94%) is explained by PC1 only, which is defined by an almost identical contribution of air CO_2,
341 RSAM, FCO2, and Earthquakes variables (see the coefficients of the first eigenvector in Table 1).
342 This suggests that a single driving mechanism controls the variations of hydrothermal fluid flux and
343 earthquakes (Fig. 6), and as such summarizes well the temporal evolution of the hydrothermal part
344 of the CFc unrest. It is worth to note that PC1 is very well correlated with the Ptot and temperature,
345 estimated using the *vapour-liquid coexistence* model (Fig. 6). We checked the reliability of this
346 result by applying PCA to a larger number of observations, i.e., considering six months means of
347 FFR variables and six months number of earthquakes, obtaining again a PC1 that explains a large
348 portion of the variance (87%) and well correlating with Ptot and temperature. These results indicate
349 that the correlation structure in the data is very strong and PCA, in the studied case, is stable also
350 with a small number of observations.
351 Summarising, PCA results support our hypothesis that increasing fluid pressure and temperature in
352 the hydrothermal system, due to an increasing input of magmatic gases, is a causal factor in
353 triggering the CFc seismicity, and is the driver for the observed escalation in hydrothermal fluid
354 release at the surface.
355 In contrast, the *no-condensation* model outputs unrealistic results, as post-2015 estimated pressures
356 are unacceptably low (< atmospheric pressure, 1 bar) and decrease over the same temporal interval
357 during which earthquake occurrence rate and surface hydrothermal fluid fluxes are both visibly
358 increasing. This mismatch indicates that the assumption that fumarolic water concentrations are
359 currently fully representative of the deep, equilibrium compositions (Moretti et al., 2017) is
360 inconsistent with the observations.
361
362 **3.5. The conceptual model of the hydrothermal system and 'hydrothermal' seismicity**
363 The conceptual model based on the *vapour-liquid coexistence* assumption is sketched in Fig. 7a
364 over a 2-D resistivity model of Solfatara, derived by AMT (AudioMagnetoTelluric) measurements
365 (Siniscalchi et al., 2019). The section is dominated by a ~2 km long vertically elongated resistivity

366 structure in axis with Solfatara. This is the core of the hydrothermal system feeding the Solfatara-
367 Pisciarelli hydrothermal sites. It is interpreted as a permeable zone that favours gas ascent from the
368 hottest and deepest portions of the system. Hot, methane-free magmatic fluids enter the base (> 2
369 km depth) of the system, mix with and vaporize meteoric liquids, and ultimately create the
370 condition for CH_4 formation at temperatures > 360°C (Caliro et al., 2007). From that zone, a gas
371 plume rises up to 0.3-0.7 km where the resistive structure is interrupted by conductive layers (green,
372 cyan and blue colours) that reflect both hydrothermal altered zones and a liquid phase-dominated
373 environment (Siniscalchi et al., 2019). It is worth noting that, assuming a hydrostatic control on
374 fluid pressure, the inferred equilibration pressures of the *vapour-liquid coexistence* model (from 30
375 to 80 bar, considering both the DP and CV redox buffers, see section 3.1.2) correspond to gas
376 equilibration depths of 0.3-0.8 km, that coincide with the top of the resistive structure (Fig. 7). Here,
377 at the interface with the overlying clay-altered zones, the gas phase is expected to accumulate and to
378 reside for a sufficient time to allow the gas phase to re-equilibrate at the local T-P conditions. From
379 that zone, the gas moves toward the surface trough fractures, shallow gas pockets and liquid bodies
380 whose existence and complex geometry has been highlighted by detailed geo-electric surveys
381 (Byrdina et al., 2014; Gresse et al., 2017; Gresse et al., 2018).
382 According to (Chiodini et al., 2016), an escalating magmatic fluid inflow at the base of the
383 hydrothermal system causes its heating and pressurization, and in turn the increase of the CO_2
384 emission at the surface and seismicity (Fig. 6). A dense earthquake cluster is observed at 0.5-1 km
385 depth (Fig. 7b and c), and since this interval nicely corresponds to the gas equilibration depths
386 inferred above (0.3-0.8 m) is here interpreted as the head of the gas front feeding the hydrothermal
387 system. Thus, our inferred Ptot increase refers to such topmost portion of this seismogenetic vertical
388 gas plume. It is also noteworthy the existence of a second, deeper (>2 km) seismicity cluster that
389 corresponds to the source area irradiating the highest magnitude earthquakes (Fig. 7b): this structure
390 has been interpreted as the root of the gas plume, in which larger events are likely caused by pulsed
391 magmatic fluid injections (e.g., Giudicepietro et al., 2020).

392 Ultimately, the close spatial correspondence between the main seismogenetic volume (0.5-1 km)
393 and the gas equilibration zone (0.3-0.8 km) supports the idea that, similarly to the seismicity
394 induced by anthropogenic fluid injection, the generalised pressurization and heating of the CFc gas
395 dominated-hydrothermal system act as the main seismicity trigger (Fig. 7b and c).
396
397 **3.6. A mass balance of the steam associated with the CO_2 emission and hydrothermal**
398 **seismicity**
399 The observed escalation in surface gas release at Solfatara and Pisciarelli is an additional evident
400 sign for increased gas transport at depth, and of a generalised gas pressure build-up at source. Using
401 the numerous data of the CO_2 emission from the target area (FCO2, Fig. 3a) we compute that the
402 total CO_2 emissions from Solfatara DDS increased from ~ 1000 t d^{-1} in 2008-2010 up to 3000-4000
403 t d^{-1} in 2019-2020 (Fig. 8). Considering that similar increments also affected the fumarolic vents
404 (Tamburello et al., 2019) we can roughly estimate the current total CO_2 emission from Solfatara-
405 Pisciarelli at ~ 5000 t d^{-1}. This flux ranks CFc among the first 8 top volcanic CO_2 emitters on Earth
406 (Fischer et al., 2019; Werner et al., 2019). Such an unusually large gas supply implies pressure-
407 build up in the gas source area (the hydrothermal system), and suggests an increased potential for
408 phreatic explosions. Volatile supply must inherently be associated with a large thermal energy
409 release (as steam and CO_2 are associated prior to condensation). We stress that since gas
410 pressurization is an exothermic process, it may itself be causing heating. In addition, the
411 pressurization of a steam-rich gas phase can induce its condensation, a process that at CFc
412 hydrothermal system is described by the *vapour-liquid coexistence* geochemical model.
413 Condensation can be shallow (forming the hot soils and mud pools that characterise the fumarolic
414 fields) or relatively deep. We attempt at establishing a steam mass balance for the hydrothermal
415 systems by dividing it into 3 components (Fig. 9a):

- the original steam emission at reservoir conditions (*reservoir emission* in Fig. 9a); this is derived by multiplying the diffuse CO_2 flux (FCO2-DDS) by the H_2O/CO_2 ratio in the gas equilibration zone (derived from P_{H2O} and P_{CO2} estimates);
- the fraction of steam condensing in the sub-surface of the DDS (*DDS condensate* in Fig. 9a); this computed by multiplying FCO2-DDS by the fumarolic H_2O/CO_2;
- the fraction of steam that condense at depth (*deep condensate* in Fig. 9a, b and c); given by the difference *reservoir emission - DDS condensate*.

It is worth to note that the inferred temporal evolution of the *deep condensate* mass matches nicely that of 'hydrothermal' seismicity (Fig. 9b and c), i.e., of the events occurred in the volume containing the hydrothermal system (see Fig. 7b and c). In our interpretation, the *deep condensate* represents the fraction of the original steam/thermal energy budget that can potentially trigger earthquakes because the condensed liquid can lubricate pre-existing fractures and because hydrothermal host rocks get hotter, increase in volume by thermal dilatation, and finally fracture as they reach a failure threshold. The total thermal energy involved in *deep condensation* from 2004 to 2020 is $\sim 4\times10^{14}$ J (computed from the latent heat of condensation), and is thus well enough to justify the observed seismicity (being 5 orders of magnitude higher than the cumulative energy of all the CFc earthquakes, $\sim 1.5\times10^{9}$ J, http://www.ov.ingv.it/ov/bollettini-mensili-campania/Bollettino_Mensile_Campi_Flegrei_2020_10.pdf).

4. Conclusions

We use a novel multidisciplinary approach to characterise the spatial-temporal evolution of the hydrothermal unrest currently affecting CFc. Use of such a multidisciplinary methodology at CFc is facilitated by the especially robust and continuous records available for both geochemical parameters (including fumarolic compositions, soil CO_2 fluxes and fluid flow related variables), and seismicity. Although these multiple dataset may not all simultaneously be available at many of the degassing restless calderas worldwide, we yet conclude our approach is general, and may find

application provided at least fumarolic gas compositions, soil flux emissions and seismic catalogues are available.

In the CFc example, a multivariate analysis shows that the different datasets share a common evolution during 2010-2020, and are fully described by a single component that explains 94% of their total variance. This component, whose values exhibit a sharp increase from 2018 onward, is well correlated with escalating pressure and temperature of the hydrothermal system inferred from geochemical modelling of fumarole composition. The P-T increase occurs in a gas-dominated zone, located at depths of < 1 km below the main hydrothermal sites, which corresponds to the main cluster of low magnitude, post 2004 earthquakes. This temporal and spatial association between hydrothermal P-T and seismicity brings compelling evidence for the role played by pressurising hydrothermal fluids in driving volcano seismicity at CFc. Our results bring evidence for the seismogenetic role played by magmatic gas injection into hydrothermal systems, and are thus of general relevance for other volcanoes in similar contexts.

Acknowledgments:

We would like to remember the researchers Roberto Cioni and Egizio Corazza who recently passed away: they began to sample and analyze Solfatara fumaroles in early 1980's, starting the Solfatara fumaroles database. We thank Bruce Christenson and an anonymous reviewer for their insightful comments. This work is part of the INGV research project LOVE-CF (Linking surface Observables to sub-Volcanic plumbing-system: a multidisciplinary approach for Eruption forecasting at Campi Flegrei caldera (Italy)).

Funding: This work was supported by MIUR, project n. PRIN2017-2017LMNLAW "Connect4Carbon". Most of the used data were acquired in the frame of the Campi Flegrei volcanic

surveillance funded by the Italian Dipartimento della Protezione Civile, Presidenza del Consiglio dei Ministri (DPC). This paper does not necessarily represent DPC official opinion and policies.

References

Aiuppa, A., Fiorani, L., Santoro, S., Parracino, S., Nuvoli, M., Chiodini, G., Minopoli, C. and Tamburello, G., 2015. New ground-based lidar enables volcanic CO_2 flux measurements. Sci. Rep., 5. https://doi.org/10.1038/srep13614.

Aiuppa, A., Tamburello, G., Di Napoli, R., Cardellini, C., Chiodini, G., Giudice, G., Grassa, F. and Pedone, M., 2013. First observations of the fumarolic gas output from a restless caldera: Implications for the current period of unrest (2005-2013) at Campi Flegrei. Geochem. Geophys. Geosys., 14(10), 4153-4169. https://doi.org/10.1002/ggge.20261.

Amoruso, A., Crescentini, L. and Sabbetta, I., 2014a. Paired deformation sources of the Campi Flegrei caldera (Italy) required by recent (1980–2010) deformation history. J. Geophys. Res., 119(2), 858-879. https://doi.org/10.1002/2013JB010392.

Amoruso, A., Crescentini, L., Sabbetta, I., De Martino , P., Obrizzo, F. and Tammaro, U., 2014b. Clues to the cause of the 2011–2013 Campi Flegrei caldera unrest, Italy, from continuous GPS data. Geophys. Res. Lett., 41, 3081-3088. https://doi.org/10.1002/2014GL059539.

Bianco, F., Del Pezzo, E., Saccorotti, G. and Ventura, G., 2004. The role of hydrothermal fluids in triggering the July–August 2000 seismic swarm at Campi Flegrei, Italy: evidence from seismological and mesostructural data. J. Volcanol. Geother. Res., 133(1), 229-246. https://doi.org/10.1016/S0377-0273(03)00400-1.

Bruno, P.P.G., Ricciardi, G.P., Petrillo, Z., Di Fiore, V., Troiano, A. and Chiodini, G., 2007. Geophysical and hydrogeological experiments from a shallow hydrothermal system at Solfatara Volcano, Campi Flegrei, Italy: Response to caldera unrest. J. Geophysi. Res, 112(B6). https://doi.org/10.1029/2006JB004383.

Byrdina, S., Vandemeulebrouck, J., Cardellini, C., Legaz, A., Camerlynck, C., Chiodini, G., Lebourg, T., Gresse, M., Bascou, P., Motos, G., Carrier, A. and Caliro, S., 2014. Relations between electrical resistivity, carbon dioxide flux, and self-potential in the shallow hydrothermal system of Solfatara (Phlegrean Fields, Italy). J. Volcanol. Geother. Res., 283, 172-182. https://doi.org/10.1016/j.jvolgeores.2014.07.010.

Caliro, S., Chiodini, G., Moretti, R., Avino, R., Granieri, D., Russo, M. and Fiebig, J., 2007. The

origin of the fumaroles of La Solfatara (Campi Flegrei, South Italy). Geochim. Cosmochim. Acta, 71(12), 3040-3055. https://doi.org/10.1016/j.gca.2007.04.007.

Caliro, S., Chiodini, G. and Paonita, A., 2014. Geochemical evidences of magma dynamics at Campi Flegrei (Italy). Geochim. Cosmochim. Acta, 132, 1-15. https://doi.org/10.1016/j.gca.2014.01.021.

Cardellini, C., Chiodini, G. and Frondini, F., 2003. Application of stochastic simulation to CO_2 flux from soil: Mapping and quantification of gas release. J. Geophys. Res., 108(B9). https://doi.org/10.1029/2002JB002165.

Cardellini, C., Chiodini, G., Frondini, F., Avino, R., Bagnato, E., Caliro, S., Lelli, M. and Rosiello, A., 2017. Monitoring diffuse volcanic degassing during volcanic unrests: The case of Campi Flegrei (Italy). Sci. Rep., 7(1). https://doi.org/10.1038/s41598-017-06941-2.

Castaldo, R., D'Auria, L., Pepe, S., Solaro, G., De Novellis, V. and Tizzani, P., 2019. The impact of crustal rheology on natural seismicity: Campi Flegrei caldera case study. Geosc. Front., 10(2), 453-466. https://doi.org/10.1016/j.gsf.2018.02.003.

Chiodini, G. and Marini, L., 1998. Hydrothermal gas equilibria: The H_2O-H_2-CO_2-CO-CH_4 system. Geochim. Cosmochim. Acta, 62(15), 2673-2687. https://doi.org/10.1016/S0016-7037(98)00181-1.

Chiodini, G., Cioni, R., Magro, G., Marini, L., Panichi, C., Raco, B. and Russo, M., 1996. Chemical and isotopic variations ofBocca Grande fumarole (Solfatara Volcano, PhlegreanFields). Acta Vulcanol., 8, 129-138.

Chiodini, G., Cioni, R., Guidi, M., Raco, B. and Marini, L., 1998. Soil CO_2 flux measurements in volcanic and geothermal areas. App. Geochem., 13(5), 543-552. https://doi.org/10.1016/S0883-2927(97)00076-0.

Chiodini, G., Frondini, F., Cardellini, C., Granieri, D., Marini, L. and Ventura, G., 2001. CO_2 degassing and energy release at Solfatara volcano, Campi Flegrei, Italy. J. Geophys. Res., 106(B8), 16213-16221. https://doi.org/10.1029/2001JB000246.

Chiodini, G., Vandemeulebrouck, J., Caliro, S., D'Auria, L., De Martino, P., Mangiacapra, A. and Petrillo, Z., 2015. Evidence of thermal-driven processes triggering the 2005-2014 unrest at campi flegrei caldera. Earth Planet. Sci. Lett., 414, 58-67. https://doi.org/10.1016/j.epsl.2015.01.012.

Chiodini, G., Paonita, A., Aiuppa, A., Costa, A., Caliro, S., De Martino, P., Acocella, V. and Vandemeulebrouck, J., 2016. Magmas near the critical degassing pressure drive volcanic unrest towards a critical state. Nat. Comm., 7. https://doi.org/10.1038/ncomms13712.

Chiodini, G., Selva, J., Del Pezzo, E., Marsan, D., De Siena, L., D'Auria, L., Bianco, F., Caliro, S.,

De Martino, P., Ricciolino, P. and Petrillo, Z., 2017a. Clues on the origin of post-2000 earthquakes at Campi Flegrei caldera (Italy). Sci. Rep., 7(1). https://doi.org/10.1038/s41598-017-04845-9.

Chiodini, G., Giudicepietro, F., Vandemeulebrouck, J., Aiuppa, A., Caliro, S., De Cesare, W., Tamburello, G., Avino, R., Orazi, M. and D'Auria, L., 2017b. Fumarolic tremor and geochemical signals during a volcanic unrest. Geology, 45(12), 1131-1134. https://doi.org/10.1130/G39447.1.

Chiodini, G., Cardellini, C., Di Luccio, F., Selva, J., Frondini, F., Caliro, S., Rosiello, A., Beddini, G. and Ventura, G., 2020. Correlation between tectonic CO_2 Earth degassing and seismicity is revealed by a 10-year record in the Apennines, Italy. Sci. Advanc., 6(35), eabc2938. https://doi.org/10.1126/sciadv.abc2938.

Cioni, R. and Corazza, E., 1981. Medium-temperature fumarolic gas sampling. Bull. Volcanol., 44(1), 23-29. https://doi.org/10.1007/BF02598186.

Cioni, R., Corazza, E. and Marini, L., 1984. The gas/steam ratio as indicator of heat transfer at the Solfatara fumaroles, Phlegraean Fields (Italy). Bull. Volcanol., 47, 295-302. https://doi.org/10.1007/BF01961560.

Costa, A., Folch, A., Macedonio, G., Giaccio, B., Isaia, R. and Smith, V.C., 2012. Quantifying volcanic ash dispersal and impact of the Campanian Ignimbrite super-eruption. Geophys. Res. Lett., 39(10). https://doi.org/10.1029/2012GL051605.

D'Amore, F. and Panichi, C., 1980. Evaluation of deep temperatures of hydrothermal systems by a new gas geothermometer. Geochim. Cosmochim. Acta, 44(3), 549-556. https://doi.org/10.1016/0016-7037(80)90051-4.

D'Auria, L., Giudicepietro, F., Aquino, I., Borriello, G., Del Gaudio, C., Lo Bascio, D., Martini, M., Ricciardi, G.P., Ricciolino, P. and Ricco, C., 2011. Repeated fluid-transfer episodes as a mechanism for the recent dynamics of Campi Flegrei caldera (1989–2010). J. Geophys. Res., 116(B4). https://doi.org/10.1029/2010JB007837.

Del Gaudio, C., Aquino, I., Ricciardi, G.P., Ricco, C. and Scandone, R., 2010. Unrest episodes at Campi Flegrei: A reconstruction of vertical ground movements during 1905–2009. J. Volcanol. Geother. Res., 195(1), 48-56. https://doi.org/10.1016/j.jvolgeores.2010.05.014.

Deutsch, C.V. and Journel, A.G., 1998. GSLIB: Geostatistical Software Library and Users Guide. Oxford Univerity Press, Oxford, New York 369 pp.

Ellsworth, W.L., 2013. Injection-Induced Earthquakes. Science, 341(6142), 1225942. https://doi.org/10.1126/science.1225942.

Endo, E.T. and Murray, T., 1991. Real-time Seismic Amplitude Measurement (RSAM): a volcano

566 monitoring and prediction tool. Bull. Volcanol., 53(7), 533-545.
567 https://doi.org/10.1007/BF00298154.
568 Everitt, B. and Hothorn, T., 2011. An introduction to applied multivariate analysis with R,
569 Springer, New York, 274 pp.
570 Farrar, C.D., Sorey, M.L., Evans, W.C., Howle, J.F., Kerr, B.D., Kennedy, B.M., King, C.Y. and
571 Southon, J.R., 1995. Forest-killing diffuse CO_2 emission at Mammoth Mountain as a sign of
572 magmatic unrest. Nature, 376(6542), 675-678. https://doi.org/10.1038/376675a0.
573 Fischer, T., Matyska, C. and Heinicke, J., 2017. Earthquake-enhanced permeability – evidence from
574 carbon dioxide release following the ML 3.5 earthquake in West Bohemia. Earth Planet. Sci.
575 Lett., 460, 60-67. https://doi.org/10.1016/j.epsl.2016.12.001.
576 Fischer, T.P., Arellano, S., Carn, S., Aiuppa, A., Galle, B., Allard, P., Lopez, T., Shinohara, H.,
577 Kelly, P., Werner, C., Cardellini, C. and Chiodini, G., 2019. The emissions of CO_2 and other
578 volatiles from the world's subaerial volcanoes. Sci. Rep., 9(1), 18716.
579 https://doi.org/10.1038/s41598-019-54682-1.
580 Giggenbach, W.F., 1980. Geothermal gas equilibria. Geochim. Cosmochim. Acta, 44, 2021-2032.
581 https://doi.org/10.1016/0016-7037(80)90200-8.
582 Giggenbach, W.F., 1987. Redox processes governing the chemistry of fumarolic gas discharges
583 from White Island, New Zealand. Appl. Geochem., 2(2), 143-161.
584 https://doi.org/10.1016/0883-2927(87)90030-8.
585 Girault, F., Adhikari, L.B., France-Lanord, C., Agrinier, P., Koirala, B.P., Bhattarai, M., Mahat,
586 S.S., Groppo, C., Rolfo, F., Bollinger, L. and Perrier, F., 2018. Persistent CO2 emissions
587 and hydrothermal unrest following the 2015 earthquake in Nepal. Nat. Commun., 9(1),
588 2956. https://doi.org/10.1038/s41467-018-05138-z.
589 Giudicepietro, F., Chiodini, G., Avino, R., Brandi, G., Caliro, S., De Cesare, W., Galluzzo, D.,
590 Esposito, A., La Rocca, A., Lo Bascio, D., Obrizzo, F., Pinto, S., Ricci, T., Ricciolino, P.,
591 Siniscalchi, A., Tramelli, A., Vandemeulebrouck, J. and Macedonio, G., 2020. Tracking
592 episodes of seismicity and gas transport in Campi Flegrei caldera trough seismic,
593 geophysical and geochemical measurements. Seismol. Res. Lett. , in press, 1-11.
594 https://doi.org/10.1785/0220200223.
595 Giudicepietro, F., Chiodini, G., Caliro, S., De Cesare, W., Esposito, A.M., Galluzzo, D., Lo Bascio,
596 D., Macedonio, G., Orazi, M., Ricciolino, P. and Vandemeulebrouck, J., 2019. Insight Into
597 Campi Flegrei Caldera Unrest Through Seismic Tremor Measurements at Pisciarelli
598 Fumarolic Field. Geochem. Geophys. Geosys., 20(11), 5544-5555.
599 https://doi.org/10.1029/2019GC008610.

600 Granieri, D., Avino, R. and Chiodini, G., 2009. Carbon dioxide diffuse emission from the soil: ten
601 years of observations at Vesuvio and Campi Flegrei (Pozzuoli), and linkages with volcanic
602 activity. Bull. Volcanol., 72(1), 103. https://doi.org/10.1007/s00445-009-0304-8.
603 Gresse, M., Vandemeulebrouck, J., Byrdina, S., Chiodini, G., Revil, A., Johnson, T.C., Ricci, T.,
604 Vilardo, G., Mangiacapra, A., Lebourg, T., Grangeon, J., Bascou, P. and Metral, L., 2017.
605 Three-Dimensional Electrical Resistivity Tomography of the Solfatara Crater (Italy):
606 Implication for the Multiphase Flow Structure of the Shallow Hydrothermal System. J.
607 Geophys. Res., 122(11), 8749-8768. https://doi.org/10.1002/2017JB014389.
608 Gresse, M., Vandemeulebrouck, J., Byrdina, S., Chiodini, G., Roux, P., Rinaldi, A.P., Wathelet, M.,
609 Ricci, T., Letort, J., Petrillo, Z., Tuccimei, P., Lucchetti, C. and Sciarra, A., 2018. Anatomy
610 of a fumarolic system inferred from a multiphysics approach. Sci. Rep., 8(1), 7580.
611 https://doi.org/10.1038/s41598-018-25448-y.
612 Hotovec-Ellis, A.J., Shelly, D.R., Hill, D.P., Pitt, A.M., Dawson, P.B. and Chouet, B.A., 2018.
613 Deep fluid pathways beneath Mammoth Mountain, California, illuminated by migrating
614 earthquake swarms. Sci. Advanc., 4(8), eaat5258. https://doi.org/10.1126/sciadv.aat5258.
615 Hubbert, M. and Rubey, W., 1959. Role of fluid pressure in mechanics of overthrust faulting. Geol.
616 Soc. Am., 70, 115-166.
617 James, G., Witten, D., Hastie, T., and Tibshirani, R., 2013. An introduction to statistical learning
618 Springer, New York, 426 pp.
619 Keranen, K.M. and Weingarten, M., 2018. Induced Seismicity. Ann. Rev. Earth Planet. Sci., 46(1),
620 149-174. https://doi.org/10.1146/annurev-earth-082517-010054.
621 Kilburn, C.R.J., De Natale, G. and Carlino, S., 2017. Progressive approach to eruption at Campi
622 Flegrei caldera in southern Italy. Nat. Comm., 8(1), 15312.
623 https://doi.org/10.1038/ncomms15312.
624 Lewicki, J.L., Hilley, G.E., Shelly, D.R., King, J.C., McGeehin, J.P., Mangan, M. and Evans, W.C.,
625 2014. Crustal migration of CO2-rich magmatic fluids recorded by tree-ring radiocarbon and
626 seismicity at Mammoth Mountain, CA, USA. Earth Planet. Sci. Lett., 390, 52-58.
627 https://doi.org/10.1016/j.epsl.2013.12.035.
628 Miller, S.A., 2013. The Role of Fluids in Tectonic and Earthquake Processes. In: R. Dmowska
629 (Editor), Advanc. Geophys. Advances in Geophysics, pp. 1-46.
630 https://doi.org/10.1016/b978-0-12-380940-7.00001-9.
631 Moretti, R., De Natale, G. and Troise, C., 2017. A geochemical and geophysical reappraisal to the
632 significance of the recent unrest at Campi Flegrei caldera (Southern Italy). Geochem.
633 Geophys. Geosys., 18(3), 1244-1269. https://doi.org/10.1002/2016GC006569.

Orsi, G., Civetta, L., Del Gaudio, C., de Vita, S., Di Vito, M.A., Isaia, R., Petrazzuoli, S.M., Ricciardi, G.P. and Ricco, C., 1999. Short-term ground deformations and seismicity in the resurgent Campi Flegrei caldera (Italy): an example of active block-resurgence in a densely populated area. J. Volcanol. Geother. Res., 91(2), 415-451. https://doi.org/10.1016/S0377-0273(99)00050-5.

Pedone, M., Aiuppa, A., Giudice, G., Grassa, F., Cardellini, C., Chiodini, G. and Valenza, M., 2014. Volcanic CO2 flux measurement at Campi Flegrei by tunable diode laser absorption spectroscopy. Bull. Volcanol., 76(4). https://doi.org/10.1007/s00445-014-0812-z.

Pfeiffer, L., Wanner, C. and Lewicki, J.L., 2018. Unraveling the dynamics of magmatic CO2 degassing at Mammoth Mountain, California. Earth Planet. Sci. Lett., 484, 318-328. https://doi.org/10.1016/j.epsl.2017.12.038.

Queißer, M., Granieri, D., Burton, M., Arzilli, F., Avino, R. and Carandente, A., 2017. Increasing CO2 flux at Pisciarelli, Campi Flegrei, Italy. Solid Earth, 8(5), 1017-1024. https://doi.org/10.5194/se-8-1017-2017.

R Core Team, 2021. R: A language and environment for statistical computing. R Foundation for Statistical Computing, Vienna, Austria.

Saccorotti, G., Petrosino, S., Bianco, F., Castellano, M., Galluzzo, D., La Rocca, M., Del Pezzo, E., Zaccarelli, L. and Cusano, P., 2007. Seismicity associated with the 2004–2006 renewed ground uplift at Campi Flegrei Caldera, Italy. Phys. Earth Planet. Inter., 165(1), 14-24. https://doi.org/10.1016/j.pepi.2007.07.006.

Selva, J., Marzocchi, W., Papale, P. and Sandri, L., 2012. Operational eruption forecasting at high-risk volcanoes: the case of Campi Flegrei, Naples. J. App. Volcanol., 1(1), 5. https://doi.org/10.1186/2191-5040-1-5.

Sibson, R.H., 1992. Implications of fault-valve behaviour for rupture nucleation and recurrence. Tectonophysics 211, 283-293. https://doi.org/10.1016/0040-1951(92)90065-E.

Siniscalchi, A., Tripaldi, S., Romano, G., Chiodini, G., Improta, L., Petrillo, Z., D'Auria, L., Caliro, S. and Avino, R., 2019. Reservoir Structure and Hydraulic Properties of the Campi Flegrei Geothermal System Inferred by Audiomagnetotelluric, Geochemical, and Seismicity Study. J. Geophys. Res., 124(6), 5336-5356. https://doi.org/10.1029/2018JB016514.

Smith, V.C., Isaia, R. and Pearce, N.J.G., 2011. Tephrostratigraphy and glass compositions of post-15 kyr Campi Flegrei eruptions: implications for eruption history and chronostratigraphic markers. Quatern. Sci. Rev., 30(25), 3638-3660. https://doi.org/10.1016/j.quascirev.2011.07.012.

Sorey, M.L., Evans, W.C., Kennedy, B.M., Farrar, C.D., Hainsworth, L.J. and Hausback, B., 1998.

668 Carbon dioxide and helium emissions from a reservoir of magmatic gas beneath Mammoth
669 Mountain, California. J. Geophys. Res., 103(7), 15303-15323.
670 https://doi.org/10.1029/98JB01389.
671 Stull, D.R., Westrum, E.F. and Sinke, G.G., 1969. The chemical thermodynamics of organic
672 compounds. Wiley, New York, 865 pp.
673 Tamburello, G., Caliro, S., Chiodini, G., De Martino, P., Avino, R., Minopoli, C., Carandente, A.,
674 Rouwet, D., Aiuppa, A., Costa, A., Bitetto, M., Giudice, G., Francofonte, V., Ricci, T.,
675 Sciarra, A., Bagnato, E. and Capecchiacci, F., 2019. Escalating CO2 degassing at the
676 Pisciarelli fumarolic system, and implications for the ongoing Campi Flegrei unrest. J.
677 Volcanol. Geother. Res., 384, 151-157. https://doi.org/10.1016/j.jvolgeores.2019.07.005.
678 Werner, C., Bergfeld, D., Farrar, C.D., Doukas, M.P., Kelly, P.J. and Kern, C., 2014. Decadal-scale
679 variability of diffuse CO2 emissions and seismicity revealed from long-term monitoring
680 (1995–2013) at Mammoth Mountain, California, USA. J. Volcanol. Geother. Res., 289, 51-
681 63. https://doi.org/10.1016/j.jvolgeores.2014.10.020.
682 Werner, C., Fischer, T.P., Aiuppa, A., Edmonds, M., Cardellini, C., Carn, S., Chiodini, G., Cottrell,
683 E., Burton, M., Shinohara, H. and Allard, P., 2019. Carbon Dioxide Emissions from
684 Subaerial Volcanic Regions: Two Decades in Review. In: B.N. Orcutt, I. Daniel and R.
685 Dasgupta (Eds.), Deep Carbon: Past to Present. Cambridge University Press, Cambridge, pp.
686 188-236. https://doi.org/10.1017/9781108677950.
687
688

689 **Table 1.** Principal Component Analysis (PCA). Results of the PCA applied to the variables FCO2,
690 RSAM, air CO_2 and earthquakes.

	Eigenvectors			
Variables	**PC1**	**PC2**	**PC3**	**PC4**
FCO_2	0.4993	0.3342	-0.7991	0.0215
RSAM	0.5100	-0.0659	0.2692	-0.8143
air CO_2	0.4914	-0.7896	-0.0134	0.3672
earthquakes	0.4992	0.5103	0.5373	0.4491
Importance of components	**PC1**	**PC2**	**PC3**	**PC4**
Variance	3.7591	0.1430	0.0736	0.0243
Proportion of variance	0.9398	0.0357	0.0184	0.0061
Cumulative proportion	0.9398	0.9755	0.9939	1.0000

691
692
693

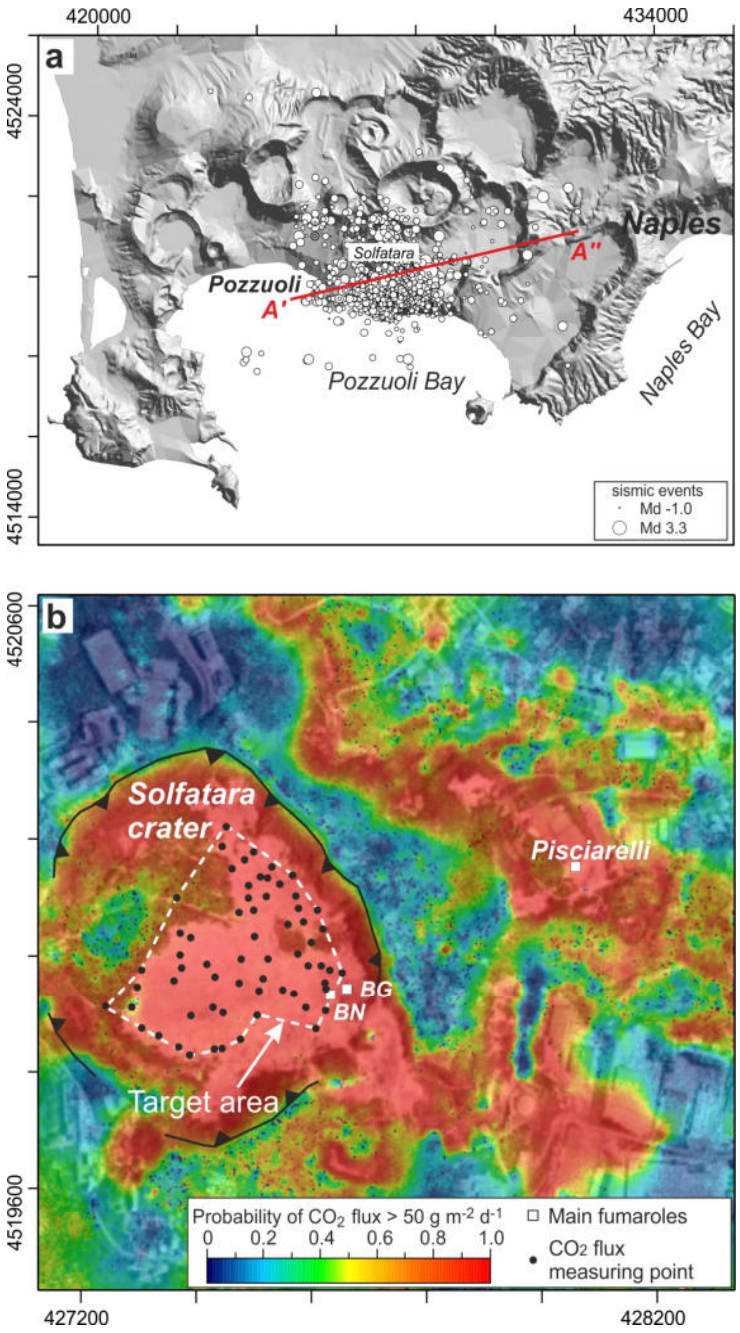

694

695 **Fig. 1.** Location map. a) Campi Flegrei caldera and location of the 2004-2020 earthquakes. The A'-
696 A'' line refers to the vertical section reported in Fig. 6. b) Map of the Solfatara diffuse degassing
697 structure (DDS) showing the locations of the target area, the monitored 63 points and the main
698 fumaroles. The map, based on 13,158 CO_2 flux measurements from 1998 to 2016 (Cardellini et al.,
699 2017), illustrates the probability that the simulated CO_2 flux is greater than 50 g m^{-2} d^{-1}, selected as
700 the threshold for a pure biogenic CO_2 flux. Coordinates are expressed in UTM-WGS84.

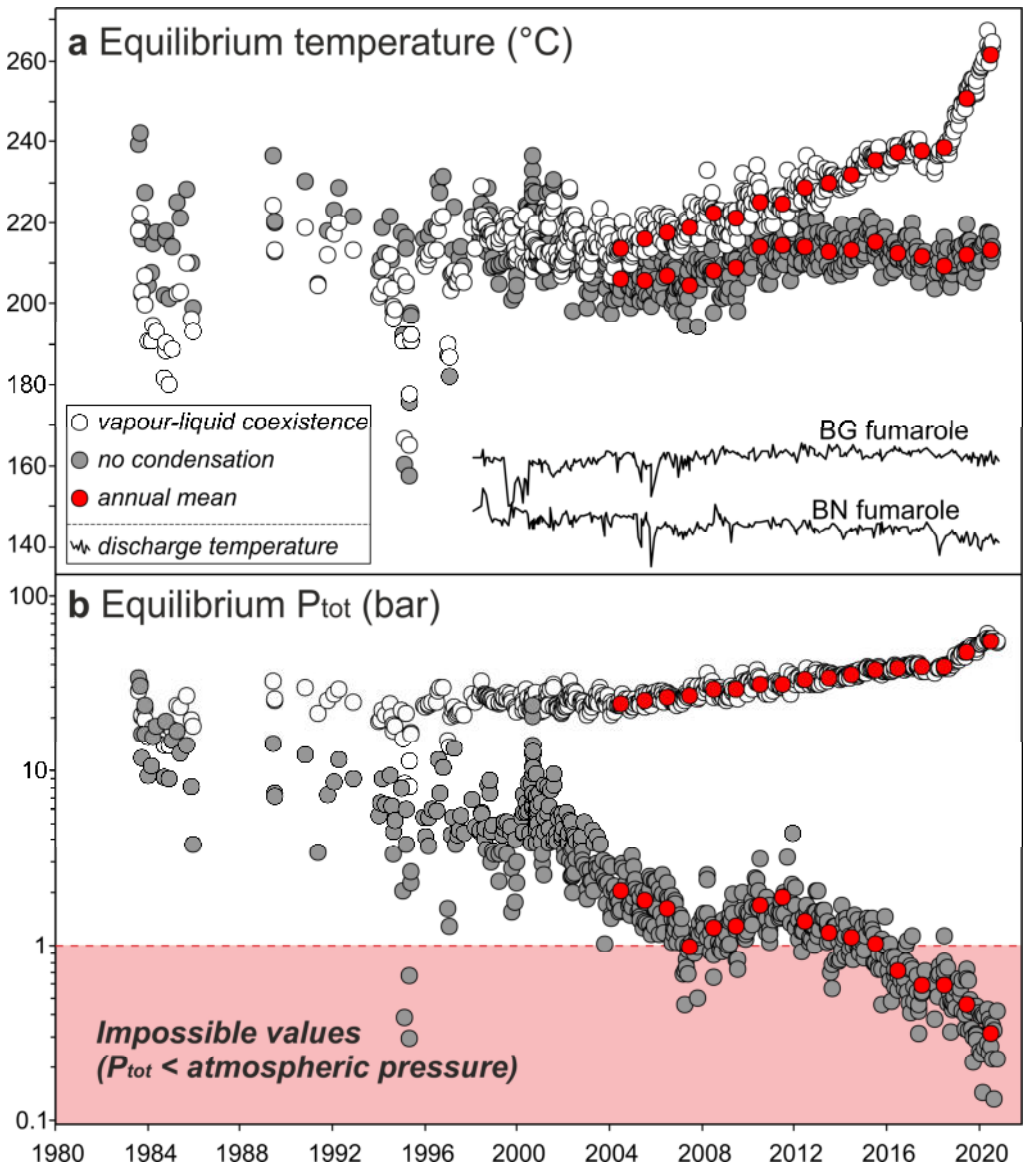

Fig. 2. T-P estimates. a) Equilibrium temperatures and b) pressures estimated with two alternative geochemical models (see the text) from the 1983-2020 compositions of BG and BN fumaroles. The discharge temperatures of the fumaroles are reported in panel a.

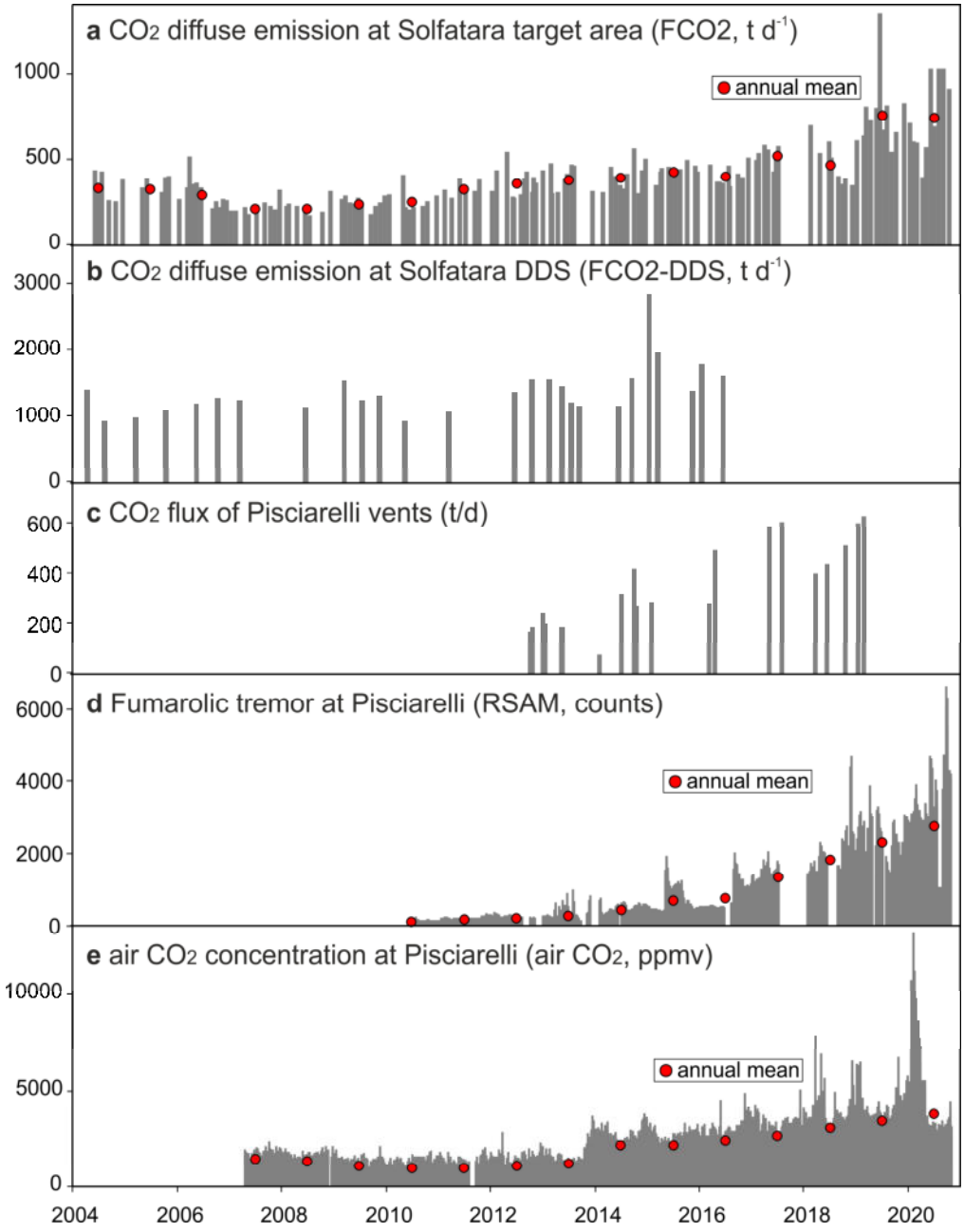

706

707 **Fig. 3.** Chronograms of the FFR variables. Annual means are reported with red symbols.

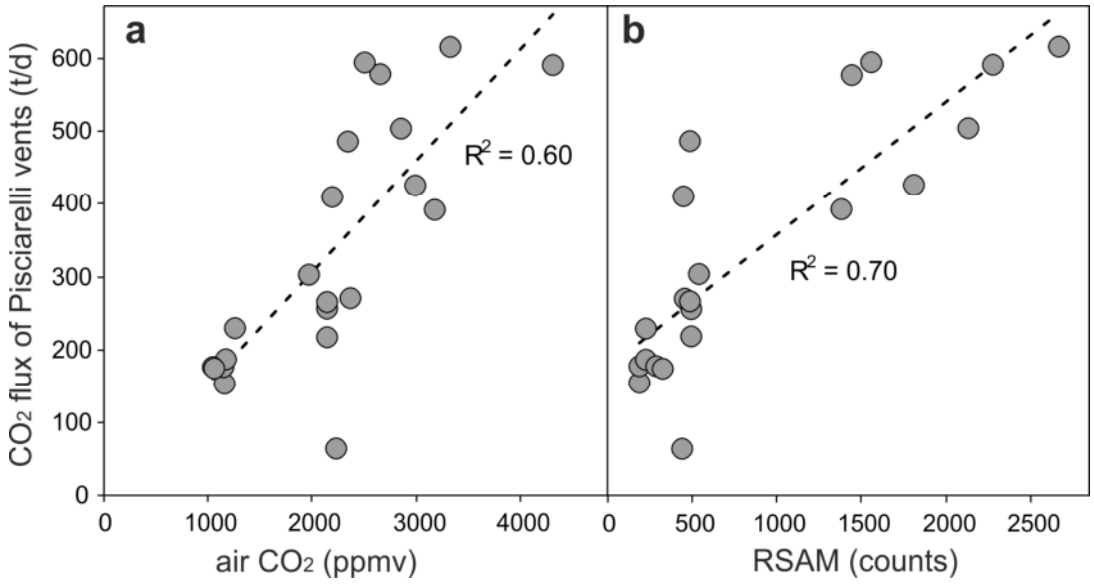

708

709

710 **Fig. 4.** Air CO_2 and RSAM vs CO_2 flux of Pisciarelli vents. RSAM and air CO_2 are reported as the

711 mean values measured at the time of the CO_2 flux campaign ± 30 days.

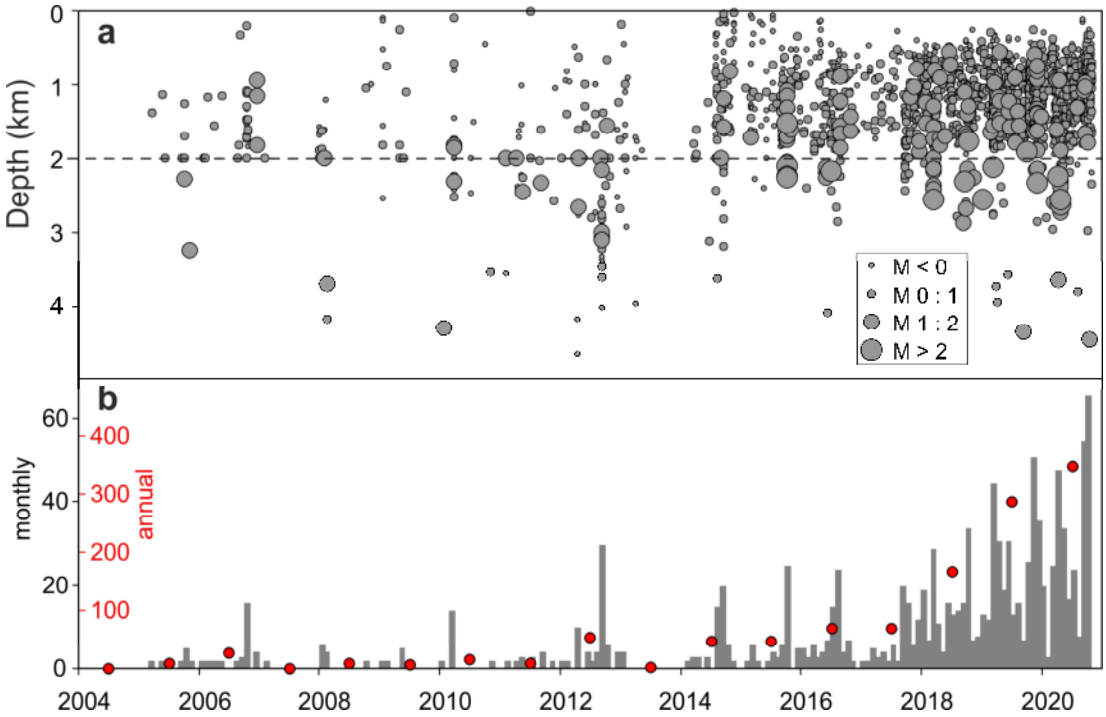

712

713

714 **Fig. 5.** CFc earthquakes from 2004 to October 2020. a) Chronogram of depths and magnitudes. b)

715 Monthly (gray histogram) and annual (red symbols) number of earthquakes with Magnitude > 0.1 ;

716 the 2020 annual number of earthquakes has been scaled over the entire year.

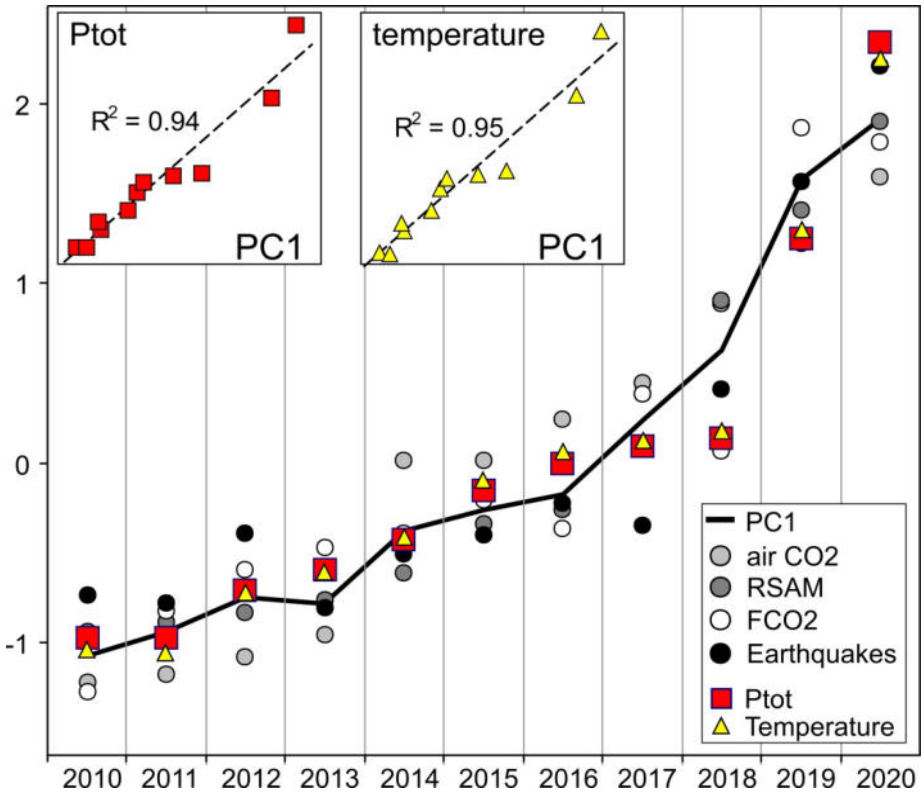

Fig. 6. Results of the PCA and Ptot. Chronograms of the z-scores of the FFR variables (air CO_2, RSAM, FCO2), earthquakes occurrence, PC1, and the Ptot-temperature estimations based on the *vapour-liquid coexistence model* (all the variables are reported as annual means; the z-score is equal to the variable minus the mean divided for the standard deviation). The FFR variables and the Earthquakes occurrence were analysed with a PCA and PC1 is the resulting main component explaining their 94% total variance. PC1 is plotted against Ptot and temperature in the insets.

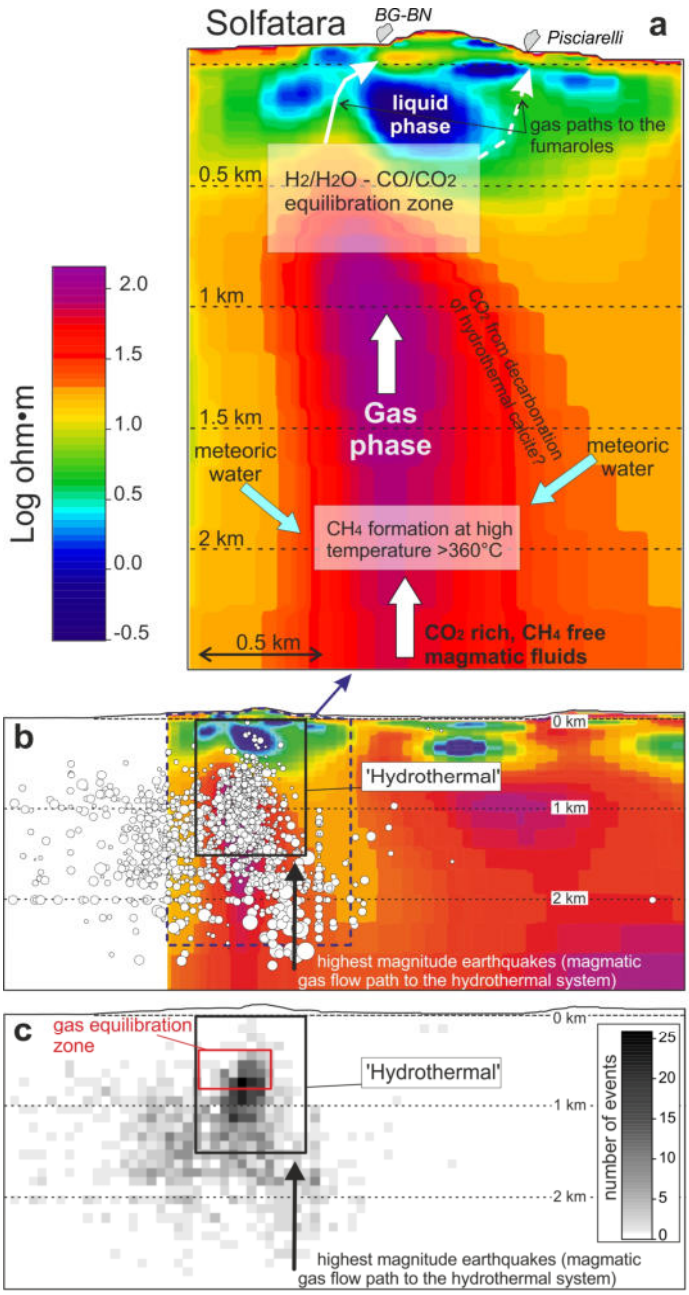

Fig. 7. Conceptual model and seismicity. a) Geochemical conceptual model of the hydrothermal system feeding the Solfatara-Pisciarelli manifestations sketched over a resistivity section (redraw from Siniscalchi et al, 2019). b) section (A'-A'' in Fig. 1A) showing the relations between earthquake location (distance < 0.6 km from the section) and resistivity. The dimension of the white circles is proportional to the magnitude of the events. c) 2 D density map of earthquakes in the A'-A'' section (computed as the number of events projected on cells of 100×100 m^2). The 'hydrothermal' box is a section of a parallelepiped of 1.2×1.2×1.5 km assumed to contain the hydrothermal system (see the text and Fig. 9).

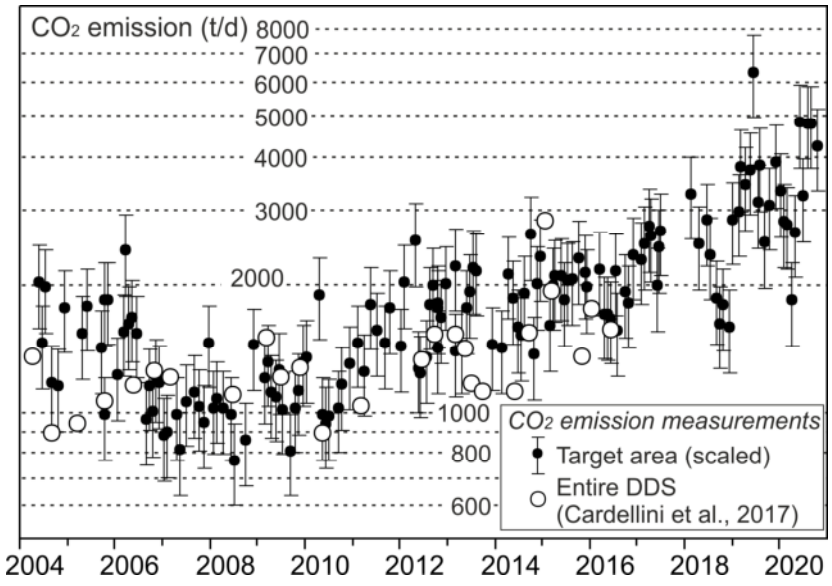

734

735

736 **Fig. 8.** CO_2 emission from diffuse degassing at Solfatara DDS during 2004-2020 The black dots
737 refer to the emission from the target area (Fig. 1 and Fig. 3a) scaled over the entire DDS. This was
738 possible by elaborating the data of the 30 campaigns reported in (Cardellini et al., 2017). From
739 these data we computed the mean ratio between the DDS emission and that from the target area
740 (4.7±1.1), that is used as correction factor (error bars refer to the standard deviation of the
741 correction factor).

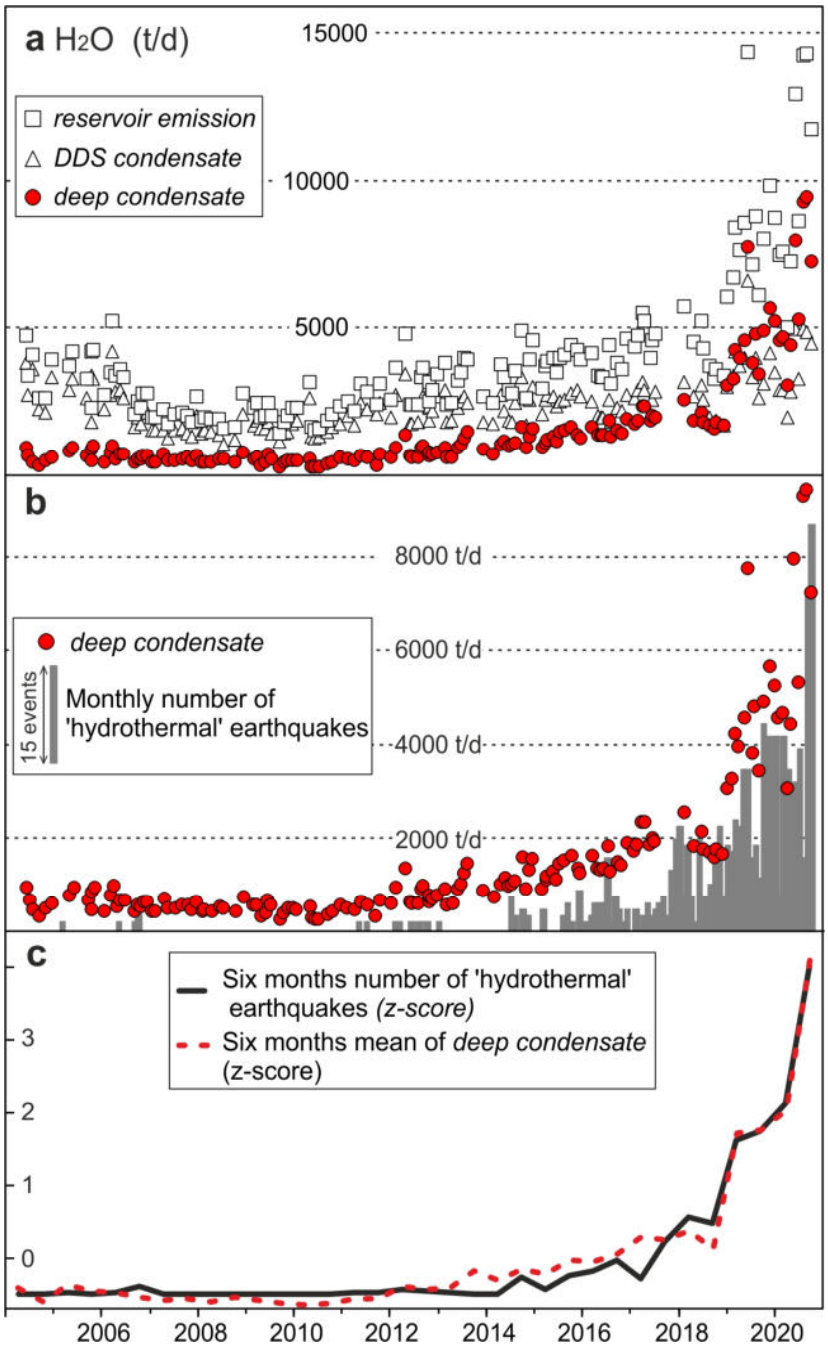

Fig. 9. Deep condensation rate and hydrothermal earthquakes occurrence. a) results of the steam mass balance involved in the degassing process (see the text). b) D*eep condensate* rate vs the monthly number of 'hydrothermal' earthquakes (grey histogram). c) Normalized 'hydrothermal' earthquakes occurrence and normalized mean of deep condensate rate (six month values). See Fig. 7 for the definition of 'hydrothermal' earthquakes.

Supplementary Material

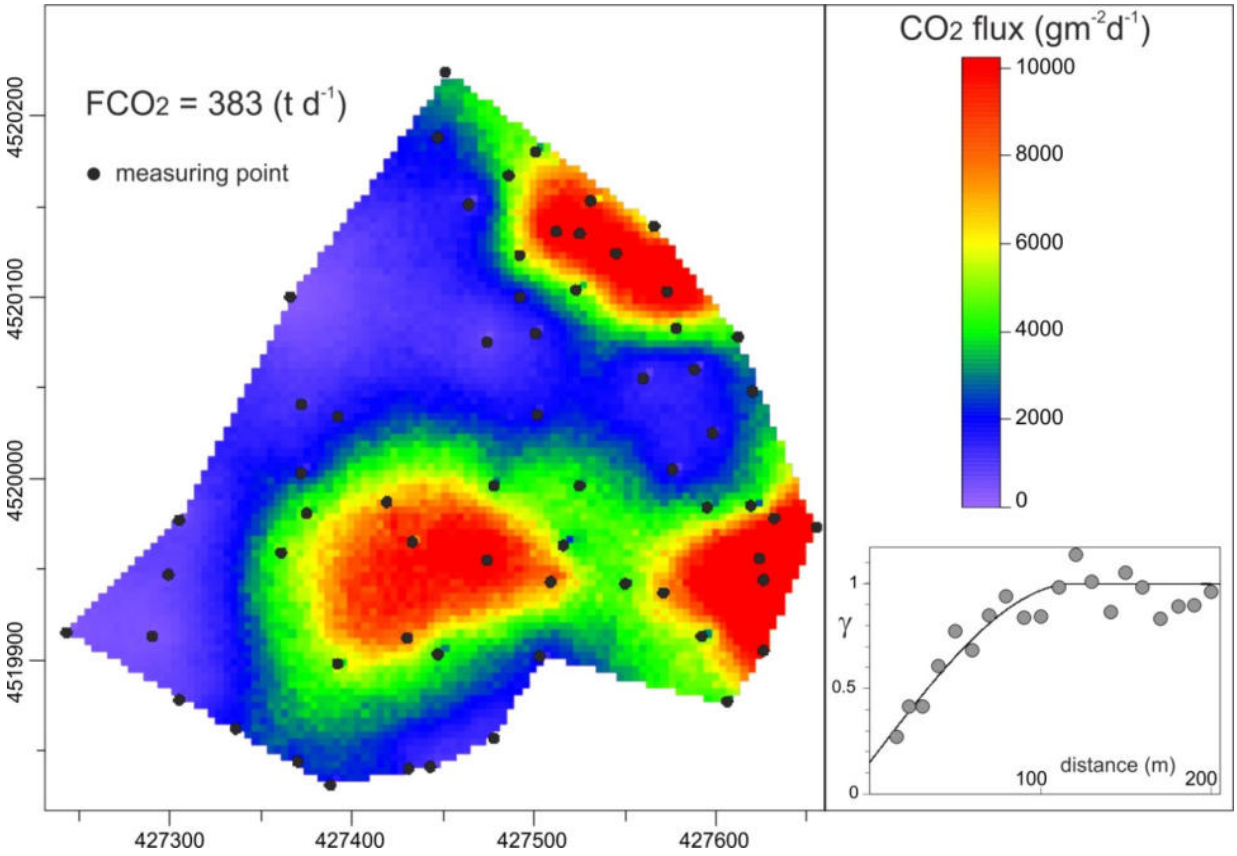

Supplementary Fig. S1. Map of the mean CO_2 flux of the target area. The map was produced by using the mean of the CO_2 fluxes measured in the 149 campaigns. In the figure is reported also the experimental variogram of the normal score of the CO_2 flux and the corresponding variogram model.

Supplementary Data File S1. Data sets: Bocca Nuova (BG) and Bocca Grande (BN) fumaroles composition; soil CO_2 flux measurements at 63 locations in the Solfatara target area; total CO_2 output target area (FCO2); Total CO_2 output form Solfatara DDS; CO_2 flux from Pisciarelli Vent; RSAM at CPIS station; Air CO_2 concentration at Pisciarelli; 2004-2020 earthquakes.